Numerical computations of the dynamics of fluidic membranes and vesicles

John W. Barrett
Department of Mathematics, Imperial College London, London SW7 2AZ, United Kingdom

Harald Garcke*
Fakultät für Mathematik, Universität Regensburg, 93040 Regensburg, Germany

Robert Nürnberg
Department of Mathematics, Imperial College London, London SW7 2AZ, United Kingdom

(Received 17 April 2015; revised manuscript received 12 October 2015; published 3 November 2015)

Vesicles and many biological membranes are made of two monolayers of lipid molecules and form closed lipid bilayers. The dynamical behavior of vesicles is very complex and a variety of forms and shapes appear. Lipid bilayers can be considered as a surface fluid and hence the governing equations for the evolution include the surface (Navier-)Stokes equations, which in particular take the membrane viscosity into account. The evolution is driven by forces stemming from the curvature elasticity of the membrane. In addition, the surface fluid equations are coupled to bulk (Navier-)Stokes equations. We introduce a parametric finite-element method to solve this complex free boundary problem and present the first three-dimensional numerical computations based on the full (Navier-)Stokes system for several different scenarios. For example, the effects of the membrane viscosity, spontaneous curvature, and area difference elasticity (ADE) are studied. In particular, it turns out, that even in the case of no viscosity contrast between the bulk fluids, the tank treading to tumbling transition can be obtained by increasing the membrane viscosity. Besides the classical tank treading and tumbling motions, another mode (called the transition mode in this paper, but originally called the vacillating-breathing mode and subsequently also called trembling, transition, and swinging mode) separating these classical modes appears and is studied by us numerically. We also study how features of equilibrium shapes in the ADE and spontaneous curvature models, like budding behavior or starfish forms, behave in a shear flow.

DOI: 10.1103/PhysRevE.92.052704 PACS number(s): 87.16.dm, 87.16.ad, 87.16.dj

I. INTRODUCTION

Lipid membranes consist of a bilayer of molecules, which have a hydrophilic head and two hydrophobic chains. These bilayers typically spontaneously form closed bag-like structures, which are called vesicles. It is observed that vesicles can attain a huge variety of shapes and some of them are similar to the biconcave shape of red blood cells. Since membranes play a fundamental role in many living systems, the study of vesicles is a very active research field in different scientific disciplines, see, e.g., Refs. [1–4]. It is the goal of this paper to present a numerical approach to study the evolution of lipid membranes. We present several computations showing quite different shapes, and the influence of fluid flow on the membrane evolution.

Since the classical papers of Canham [5] and Helfrich [6], there has been a lot of work with the aim of describing equilibrium membrane shapes with the help of elastic membrane energies. Canham [5] and Helfrich [6] introduced a bending energy for a nonflat membrane, which is formulated with the help of the curvature of the membrane. In the class of fixed topologies the relevant energy density, in the simplest situation, is proportional to the square of the mean curvature $\varkappa$. The resulting energy functional is called the Willmore energy. When computing equilibrium membrane shapes one has to take constraints into account. Lipid membranes have a very small compressibility and hence can safely be modeled as locally incompressible. In addition, the presence of certain molecules in the surrounding fluid, for which the membrane is impermeable, leads to an osmotic pressure, which results in a constraint for the volume enclosed by the membrane. The minimal energetic model for lipid membranes consists of the Willmore mean curvature functional together with enclosed volume and surface area constraints. Already this simple model leads to quite different shapes, including the biconcave red blood cell shapes; see Ref. [1].

Helfrich [6] introduced a variant of the Willmore energy, with the aim of modeling a possible asymmetry of the bilayer membrane. Helfrich [6] studied the functional $\int(\varkappa-\overline{\varkappa})^2$, where $\overline{\varkappa}$ is a fixed constant, the so-called spontaneous curvature. It is argued that the origin of the spontaneous curvature is, e.g., a different chemical environment on both sides of the membrane. We refer to Refs. [7] and [8] for a recent discussion, and for experiments in situations that lead to spontaneous curvature effects due to the chemical structure of the bilayer.

Typically there is yet another asymmetry in the bilayer leading to a signature in the membrane architecture. This results from the fact that the two membrane layers have a different number of molecules. Since the exchange of molecules between the layers is difficult, an imbalance is conserved during a possible shape change. The total area difference between the two layers is proportional to $M=\int\varkappa$. Several models have been proposed, which describe the difference in the total number of molecules in the two layers with the help of the integrated mean curvature. The bilayer coupling model, introduced by Svetina and coworkers [9–11], assumes that the

*harald.garcke@ur.de

area per lipid molecule is fixed and assumes that there is no exchange of molecules between the two layers. Hence the total areas of the two layers are fixed, and on assuming that the two layers are separated by a fixed distance, one obtains, to the order of this distance, that the area difference can be approximated by the integrated mean curvature; see Refs. [9–11]. We note that a spontaneous curvature contribution is irrelevant in the bilayer coupling model as this would only add a constant to the energy as the area and integrated mean curvature are fixed.

Miao *et al.* [12] noted that in the bilayer coupling model budding always occurs continuously, which is inconsistent with experiments. They hence studied a model in which the area of the two layers are not fixed but can expand or compress under stress. Given a relaxed initial area difference ΔA_0, the total area difference ΔA, which is proportional to the integrated mean curvature, can deviate from ΔA_0. However, the total energy now has a contribution that is proportional to $(\Delta A - \Delta A_0)^2$. This term describes the elastic area difference stretching energy; see Refs. [1,12], and hence one has to pay a price energetically to deviate from the relaxed area difference.

It is also possible to combine the area difference elasticity (ADE) model with a spontaneous curvature assumption; see Miao *et al.* [12] and Seifert [1]. However, the resulting energetical model is equivalent to an ADE model with a modified ΔA_0; see Ref. [1] for a more detailed discussion.

It has been shown that the bilayer coupling (BC) model and the ADE model lead to a multitude of shapes, which also have been observed in experiments with vesicles. Beside others, the familiar discocyte shapes (including the "shape" of a red blood cell), stomatocyte shapes, prolate shapes, and pear-like shapes have been observed. In addition, the budding of membranes can be described, as well as more exotic shapes, like starfish vesicles. Moreover, higher genus shapes appear as global or local minima of the energies discussed above. We refer to Refs. [1,12–15] for more details on the possible shapes appearing, when minimizing the energies in the ADE and BC models.

Configurational changes of vesicles and membranes cannot be described by energetical considerations alone, but have to be modeled with the help of appropriate evolution laws. Several authors considered an L^2-gradient flow dynamics of the curvature energies discussed above. Pure Willmore flow has been studied in Refs. [16–21], where the last two papers use a phase field formulation of the Willmore problem. Some authors also took other aspects, such as constraints on volume and area [19,22,23], as well as a constraint on the integrated mean curvature [19,20], into account. The effect of different lipid components in an L^2-gradient flow approach of the curvature energy has been studied in Refs. [24–30].

The above mentioned works considered a global constraint on the surface area. The membrane, however, is locally incompressible and hence a local constraint on the evolution of the membrane molecules should be taken into account. Several authors included the local inextensibility constraint by introducing an inhomogeneous Lagrange multiplier for this constraint on the membrane. This approach has been used within the context of different modeling and computational strategies such as the level set approach [31–34], the phase field approach [35–37], the immersed boundary method [38–40], the interfacial spectral boundary element method [41], and the boundary integral method [42].

The physically most natural way to consider the local incompressibility constraint makes use of the fact that the membrane itself can be considered as an incompressible surface fluid. This implies that a surface Navier-Stokes system has to be solved on the membrane. The resulting set of equations has to take forces stemming from the surrounding fluid and from the membrane elasticity into account. In total, bulk Navier-Stokes equations coupled to surface Navier-Stokes equations have to be solved. As the involved Reynolds numbers for vesicles are typically small one can often replace the full Navier-Stokes equations by the Stokes systems on the surface and in the bulk. The incompressibility condition in the bulk (Navier-)Stokes equations naturally leads to conservation of the volume enclosed by the membrane and the incompressibility condition on the surface leads a conservation of the membrane's surface area. A model involving coupled bulk-surface (Navier-)Stokes equations has been proposed by Arroyo and DeSimone [43], and it is this model that we want to study numerically in this paper.

Introducing forces resulting from membrane energies in fluid flow models has been studied numerically before by different authors [31–33,36,37,40]. However, typically these authors studied simplified models, and either volume or surface constraints were enforced by Lagrange multipliers. In addition, either just the bulk or just the surface (Navier-)Stokes equations have been solved. The only work considering simultaneously bulk and surface Navier-Stokes equations are Arroyo *et al.* [44] and Barrett *et al.* [45], 46], where the former work is restricted to axisymmetric situations. In the present paper we are going to make use of the numerical method introduced in Ref. [46]; see also Ref. [45].

The paper is organized as follows. In the next section we precisely state the mathematical model, consisting of the curvature elasticity model together with a coupled bulk-surface (Navier-)Stokes system. In Sec. III we introduce our numerical method, which consists of an unfitted parametric finite-element method for the membrane evolution. The curvature forcing is discretized and coupled to the Navier-Stokes system in a stable way using the finite-element method for the fluid unknowns. Numerical computations in Sec. IV demonstrate that we can deal with a variety of different membrane shapes and flow scenarios. In particular, we will study what influence the membrane viscosity, the ADE, and the spontaneous curvature have on the evolution of bilayer membranes in shear flow. We finish with some conclusions.

II. A CONTINUUM MODEL FOR FLUIDIC MEMBRANES

We consider a continuum model for the evolution of biomembranes and vesicles, which consists of a curvature elasticity model for the membrane and the Navier-Stokes equations in the bulk and on the surface. The model is based on a paper by Arroyo and DeSimone [43], where in addition we also allow the curvature energy model to be an area difference elasticity model. We first introduce the curvature elasticity model and then describe the coupling to the surface and bulk Navier-Stokes equations.

The thickness of the lipid bilayer in a vesicle is typically three to four orders of magnitude smaller than the typical size of the vesicle. Hence, the membrane can be modeled as a two-dimensional surface Γ in $\mathbb{R}^3$. Given the principal curvatures $\varkappa_1$ and $\varkappa_2$ of Γ, one can define the mean curvature

$$\varkappa = \varkappa_1 + \varkappa_2$$

and the Gauß curvature

$$K = \varkappa_1 \, \varkappa_2$$

(as often in differential geometry we choose to take the sum of the principal curvatures as the mean curvature, instead of its mean value). The classical works of Canham [5] and Helfrich [6] derive a local bending energy, with the help of an expansion in the curvature, and they obtain

$$\int_\Gamma \left(\frac{\alpha}{2} \, \varkappa^2 + \alpha_G \, K \right) ds \tag{1}$$

as the total energy of a symmetric membrane. The parameters α,α_G have the dimension of energy and are called the bending rigidity α and the Gaussian bending rigidity α_G. If we consider closed membranes with a fixed topology, the term $\int_\Gamma K \, ds$ is constant and hence we will neglect the Gaussian curvature term in what follows.

As discussed above, the total area difference ΔA of the two lipid layers is, to first order, proportional to

$$M(\Gamma) = \int_\Gamma \varkappa \, ds.$$

Taking now into account that there is an optimal area difference ΔA_0, the authors in Refs. [47–49] added a term proportional to

$$[M(\Gamma) - M_0]^2$$

to the curvature energy, where M_0 is a fixed constant that is proportional to the optimal area difference.

For nonsymmetric membranes a certain mean curvature $\overline{\varkappa}$ can be energetically favorable. Then the elasticity energy Eq. (1) is modified to

$$\int_\Gamma \left(\frac{\alpha}{2} \, (\varkappa - \overline{\varkappa})^2 + \alpha_G \, K \right) ds.$$

The constant $\overline{\varkappa}$ is called spontaneous curvature. Taking into account that $\int_\Gamma \alpha_G \, K \, ds$ does not change for an evolution within a fixed topology class, the most general bending energy that we use in this paper is given by $\alpha \, E(\Gamma)$, with the dimensionless energy

$$E(\Gamma) = \frac{1}{2} \int_\Gamma (\varkappa - \overline{\varkappa})^2 \, ds + \frac{\beta}{2} \, [M(\Gamma) - M_0]^2, \tag{2}$$

where β has the dimension $(\frac{1}{\text{length}})^2$.

We now consider a continuum model for the fluid flow on the membrane and in the bulk, inside and outside of the membrane. We assume that the closed, time-dependent membrane $[\Gamma(t)]_{t \geqslant 0}$ lies inside a spatial domain $\Omega \subset \mathbb{R}^3$. For all times the membrane separates Ω into an inner domain $\Omega_-(t)$ and an outer domain $\Omega_+(t)$. Denoting by $\vec{u}$ the fluid velocity and by p the pressure, the bulk stress tensor is given by $\underline{\underline{\sigma}} = 2 \, \mu \, \underline{\underline{D}}(\vec{u}) - p \, \underline{\underline{\mathrm{Id}}}$, with $\underline{\underline{D}}(\vec{u}) = \frac{1}{2} \, [\vec{\nabla} \, \vec{u} + (\vec{\nabla} \, \vec{u})^T]$ being the bulk rate-of-strain tensor. We assume that the Navier-Stokes system,

$$\rho \, [\vec{u}_t + (\vec{u} \cdot \vec{\nabla}) \, \vec{u}] - \vec{\nabla} \cdot \underline{\underline{\sigma}} = 0 \, , \quad \vec{\nabla} \cdot \vec{u} = 0,$$

holds in $\Omega_-(t)$ and $\Omega_+(t)$. Here ρ and μ are the density and dynamic viscosity of the fluid, which can take different (constant) values $\rho_\pm$, $\mu_\pm$ in $\Omega_\pm(t)$. Arroyo and DeSimone [43] used the theory of interfacial fluid dynamics, which goes back to Scriven [50], to introduce a relaxation dynamics for fluidic membranes. In this model the fluid velocity is assumed to be continuous across the membrane, the membrane is moved in the normal direction with the normal velocity of the bulk fluid and, in addition, the surface Navier-Stokes equations

$$\rho_\Gamma \, \partial_t^\bullet \, \vec{u} - \vec{\nabla}_s \cdot \underline{\underline{\sigma}}_\Gamma = [\underline{\underline{\sigma}}]_-^+ \, \vec{\nu} + \alpha \, \vec{f}_\Gamma \, , \quad \vec{\nabla}_s \cdot \vec{u} = 0$$

have to hold on $\Gamma(t)$. Here ρ_Γ is the surface material density, $\partial_t^\bullet$ is the material derivative and $\vec{\nabla}_s$ is the gradient operator on the surface. The surface stress tensor is given by

$$\underline{\underline{\sigma}}_\Gamma = 2 \, \mu_\Gamma \, \underline{\underline{D}}_s(\vec{u}) - p_\Gamma \, \underline{\underline{\mathcal{P}}}_\Gamma,$$

where p_Γ is the surface pressure, μ_Γ is the surface shear viscosity, $\underline{\underline{\mathcal{P}}}_\Gamma$ is the projection onto the tangent space, and

$$\underline{\underline{\mathcal{D}}}_s(\vec{u}) = \tfrac{1}{2} \, \underline{\underline{\mathcal{P}}}_\Gamma \, [\vec{\nabla}_s \, \vec{u} + (\vec{\nabla}_s \, \vec{u})^T] \, \underline{\underline{\mathcal{P}}}_\Gamma$$

is the surface rate-of-strain tensor. Furthermore, the term $[\underline{\underline{\sigma}}]_-^+ \, \vec{\nu} = \underline{\underline{\sigma}}_+ \, \vec{\nu} - \underline{\underline{\sigma}}_- \, \vec{\nu}$ is the force exerted by the bulk on the membrane, where $\vec{\nu}$ denotes the exterior unit normal to $\Omega_-(t)$. The remaining term $\alpha \, \vec{f}_\Gamma$ denotes the forces stemming from the elastic bending energy. These forces are given by the first variation of the bending energy $\alpha \, E[\Gamma(t)]$; see Refs. [1,43]. It turns out that $\vec{f}_\Gamma$ points in the normal direction, i.e., $\vec{f}_\Gamma = f_\Gamma \, \vec{\nu}$, and we obtain (see Refs. [1,51])

$$\begin{aligned} f_\Gamma = &-\Delta_s \, \varkappa - (\varkappa - \overline{\varkappa}) \, |\vec{\nabla}_s \, \vec{\nu}|^2 + \tfrac{1}{2} \, (\varkappa - \overline{\varkappa})^2 \, \varkappa \\ &+ \beta \, (M(\Gamma) - M_0) \, (|\vec{\nabla}_s \, \vec{\nu}|^2 - \varkappa^2) \quad \text{on } \Gamma(t). \end{aligned}$$

Here Δ_s is the surface Laplace operator, $\vec{\nabla}_s \, \vec{\nu}$ is the Weingarten map, and $|\vec{\nabla}_s \, \vec{\nu}|^2 = \varkappa_1^2 + \varkappa_2^2$. Assuming, e.g., no-slip boundary conditions on $\partial\Omega$, the boundary of Ω, we obtain that the total energy can only decrease; i.e.,

$$\begin{aligned} &\frac{d}{dt} \left[\int_\Omega \frac{\rho}{2} \, |\vec{u}|^2 \, dx + \frac{\rho_\Gamma}{2} \int_\Gamma |\vec{u}|^2 \, ds + \alpha \, E(\Gamma) \right] \\ &\quad = -2 \left[\int_\Omega \mu \, |\underline{\underline{D}}(\vec{u})|^2 \, dx + \mu_\Gamma \int_\Gamma |\underline{\underline{D}}_s(\vec{u})|^2 \, ds \right] \leqslant 0 \, . \end{aligned} \tag{3}$$

We now nondimensionalize the problem. We choose a time scale $\tilde{t}$, a length scale $\tilde{x}$, and the resulting velocity scale $\tilde{u} = \tilde{x}/\tilde{t}$. Then we define the bulk and surface Reynolds numbers,

$$\mathrm{Re} = \tilde{x} \, \rho_+ \, \tilde{u}/\mu_+ \quad \text{and} \quad \mathrm{Re}_\Gamma = \tilde{x} \, \rho_\Gamma \, \tilde{u}/\mu_\Gamma,$$

the bulk and surface pressure scales,

$$\tilde{p} = \mu_+/\tilde{t} \quad \text{and} \quad \tilde{p}_\Gamma = \mu_+ \, \tilde{x}/\tilde{t}^2 = \mu_+ \, \tilde{u} \, ,$$

and

$$\rho^* = \rho/\rho_+ = \begin{cases} 1 & \text{in } \Omega_+ \\ \rho_-/\rho_+ & \text{in } \Omega_- \end{cases},$$

$$\mu^* = \mu/\mu_+ = \begin{cases} 1 & \text{in } \Omega_+ \\ \Lambda & \text{in } \Omega_- \end{cases}, \quad \Lambda = \mu_-/\mu_+ ,$$
$$\mu_\Gamma^* = \mu_\Gamma/(\mu_+ \tilde{x}) ,$$

as well as the new independent variables $\widehat{x} = x/\tilde{x}$, $\widehat{t} = t/\tilde{t}$. For the unknowns,

$$\widehat{\vec{u}} = \vec{u}/\tilde{u} \ , \ \widehat{p} = p/\tilde{p} \ , \ \widehat{p_\Gamma} = p_\Gamma/\tilde{p}_\Gamma ,$$

we now obtain the following set of equations (on dropping the $\widehat{\ }$ notation for the new variables for ease of exposition):

$$\begin{aligned} &\mathrm{Re}\, \rho^* (\vec{u}_t + (\vec{u} \cdot \vec{\nabla}) \vec{u}) - \mu^* \Delta \vec{u} + \vec{\nabla} p = 0 \quad \text{in } \Omega_\pm(t) , \\ &\mathrm{Re}_\Gamma \mu_\Gamma^* \partial_t^\bullet \vec{u} - \vec{\nabla}_s \cdot (2 \mu_\Gamma^* \underline{\underline{D}}_s(\vec{u}) - p_\Gamma \underline{\underline{\mathcal{P}}}_\Gamma) \\ &\qquad = \left[2 \mu^* \underline{\underline{D}}(\vec{u}) - p \underline{\underline{\mathrm{Id}}}\right]_-^+ \vec{\nu} + \alpha^* \vec{f}_\Gamma^* \quad \text{on } \Gamma(t) , \end{aligned} \tag{4}$$

with $\vec{f}_\Gamma^* = f_\Gamma^* \vec{\nu}$,

$$\begin{aligned} f_\Gamma^* = &-\Delta_s \varkappa - (\varkappa - \overline{\varkappa}^*) |\vec{\nabla}_s \vec{\nu}|^2 + \tfrac{1}{2} (\varkappa - \overline{\varkappa}^*)^2 \varkappa \\ &+ \beta^* (M(\Gamma) - M_0^*) (|\vec{\nabla}_s \vec{\nu}|^2 - \varkappa^2) \quad \text{on } \Gamma(t) , \end{aligned} \tag{5}$$

$\alpha^* = \alpha/(\mu_+ \tilde{u} \tilde{x}^2)$ and $\overline{\varkappa}^* = \tilde{x} \overline{\varkappa}$, $M_0^* = M_0/\tilde{x}$, $\beta^* = \tilde{x}^2 \beta$. We remark that the Reynolds numbers for the two regions in the bulk are given by Re and $\mathrm{Re}\, \rho^*/\mu^*$, respectively, and that they will, in general, differ in the case of a viscosity contrast between the inner and outer fluid. In addition to the above equations, we of course also require that $\vec{u}$ has zero divergence in the bulk and that the surface divergence of $\vec{u}$ vanishes on Γ.

Typical values for the bulk dynamic viscosity μ are around 10^{-3}–10^{-2} $\frac{\mathrm{kg}}{\mathrm{s\,m}}$ (see Refs. [4,43,52]), whereas the surface shear viscosity typically is about 10^{-9}–10^{-8} $\frac{\mathrm{kg}}{\mathrm{s}}$ (see Refs. [4,30,53]). The bending modulus α is typically 10^{-20}–10^{-19} $\frac{\mathrm{kg\,m^2}}{\mathrm{s^2}}$ (see Refs. [30,52,53]).

The term $\mu_\Gamma^* = \mu_\Gamma/(\mu_+ \tilde{x})$ in Eq. (4) suggests choosing the length scale

$$\tilde{x} = \mu_\Gamma/\mu_+ \quad \Longleftrightarrow \quad \mu_\Gamma^* = 1.$$

As $\alpha^* = \alpha/(\mu_+ \tilde{u} \tilde{x}^2) = \alpha \tilde{t}/(\mu_+ \tilde{x}^3)$ appears in Eq. (4), we choose the time scale

$$\tilde{t} = \mu_+ \tilde{x}^3/\alpha.$$

Choosing

$$\mu_\Gamma = 5 \times 10^{-9} \frac{\mathrm{kg}}{\mathrm{s}}, \ \mu_+ = 10^{-3} \frac{\mathrm{kg}}{\mathrm{s\,m}}, \ \alpha = 10^{-19} \frac{\mathrm{kg\,m^2}}{\mathrm{s^2}},$$

see, e.g., Ref. [43], we obtain the length scale 5×10^{-6} m and the time scale 1.25 s, which are typical scales in experiments. With these scales for length and time together with values of $\sim 10^3\ \mathrm{kg/m^3}$ for the bulk density and $\sim 10^{-6}\ \mathrm{kg/m^2}$ for the surface densities, we obtain for the bulk and surface Reynolds numbers

$$\mathrm{Re} \approx 10^{-5} \quad \text{and} \quad \mathrm{Re}_\Gamma \approx 10^{-8},$$

and hence we will set the Reynolds numbers to zero in this paper. We note that it is straightforward to also consider positive Reynolds numbers in our numerical algorithm; see Refs. [45,46] for details. Together with the other observations above, we then obtain the following reduced set of equations:

$$\begin{aligned} &- \mu^* \Delta \vec{u} + \vec{\nabla} p = 0 \quad \text{in } \Omega_\pm(t) , \\ &- 2 \vec{\nabla}_s \cdot \underline{\underline{D}}_s(\vec{u}) + \vec{\nabla}_s \cdot (p_\Gamma \underline{\underline{\mathcal{P}}}_\Gamma) \\ &\qquad = [2 \mu^* \underline{\underline{D}}(\vec{u}) - p \underline{\underline{\mathrm{Id}}}]_-^+ \vec{\nu} + \alpha^* \vec{f}_\Gamma^* \quad \text{on } \Gamma(t). \end{aligned} \tag{6}$$

A downside of the scaling used to obtain Eq. (6) is that the surface viscosity no longer appears as an independent parameter. However, studying the effect of the surface viscosity, e.g., on the tank treading to tumbling transition in shearing experiments, is one of the main focuses of this paper. It is for this reason that we also consider the following alternative scaling, when suitable length and velocity scales are at hand. For example, we may choose the length scale $\tilde{x}$ based on the (fixed) size of the membrane and a velocity scale $\tilde{u}$ based on appropriate boundary velocity values. In this case we obtain from Eq. (4), for small Reynolds numbers, the following set of equations:

$$\begin{aligned} &- \mu^* \Delta \vec{u} + \vec{\nabla} p = 0 \quad \text{in } \Omega_\pm(t), \\ &- \vec{\nabla}_s \cdot [2 \mu_\Gamma^* \underline{\underline{D}}_s(\vec{u}) - p_\Gamma \underline{\underline{\mathcal{P}}}_\Gamma] \\ &\qquad = [2 \mu^* \underline{\underline{D}}(\vec{u}) - p \underline{\underline{\mathrm{Id}}}]_-^+ \vec{\nu} + \alpha^* \vec{f}_\Gamma^* \quad \text{on } \Gamma(t). \end{aligned} \tag{7}$$

Note that here three nondimensional parameters remain: μ_Γ^*, Λ, and α^*. Here μ_Γ^* compares the surface shear viscosity to the bulk shear viscosity, Λ is the bulk viscosity ratio, and α^* is an inverse capillary number, which describes the ratio of characteristic membrane stresses to viscous stresses. Clearly, the system Eq. (6) corresponds to Eq. (7) with $\mu_\Gamma^* = 1$. Hence, from now on, we will only consider the scaling Eq. (7) in detail.

Of course, the system Eq. (7) needs to be supplemented with a boundary condition for $\vec{u}$ or $\underline{\underline{\sigma}}$, and with an initial condition for $\Gamma(0)$. For the former we partition the boundary $\partial\Omega$ of Ω into $\partial_1\Omega$, where we prescribe a fixed velocity $\vec{u} = \vec{g}$, and $\partial_2\Omega$, where we prescribe the stress-free condition $\underline{\underline{\sigma}}\, \vec{n} = \vec{0}$, with $\vec{n}$ denoting the outer normal to Ω.

We note that our nondimensionalization may be different to others presented in the literature. Often the length scale $a = (\frac{\mathcal{A}(0)}{4\pi})^{\frac{1}{2}}$ is chosen, where $\mathcal{A}(0)$ denotes the surface area of the vesicle at time zero; see, e.g., Ref. [54]. Our length scale $\tilde{x}$ may lead to simulations with $\mathcal{A}(0) = 4\pi S^2$, with $S > 0$, so that our nondimensional parameters in Eq. (7) correspond to the nondimensional values for a fixed length scale $\tilde{x} = a$ as follows:

$$\mathcal{M} = \frac{\mu_\Gamma}{\mu_+ a} = \frac{\mu_\Gamma^*}{S}, \ a \overline{\varkappa} = S \overline{\varkappa}^*, \ \mathrm{Ca} = \frac{\mu_+ \tilde{u} a^3}{\tilde{x} \alpha} = \frac{S^3}{\alpha^*}. \tag{8}$$

III. NUMERICAL APPROXIMATION

The numerical computations in this paper have been performed with a finite-element approximation introduced by the authors in Ref. [46]. The approach discretizes the bulk and surface degrees of freedom independently. In particular, the surface mesh is not a restriction of the bulk mesh. The bulk degrees of freedoms $\vec{u}$ and p are discretized with the lowest order Taylor-Hood element, P2-P1, in our numerical computations. The evolution of the membrane is tracked

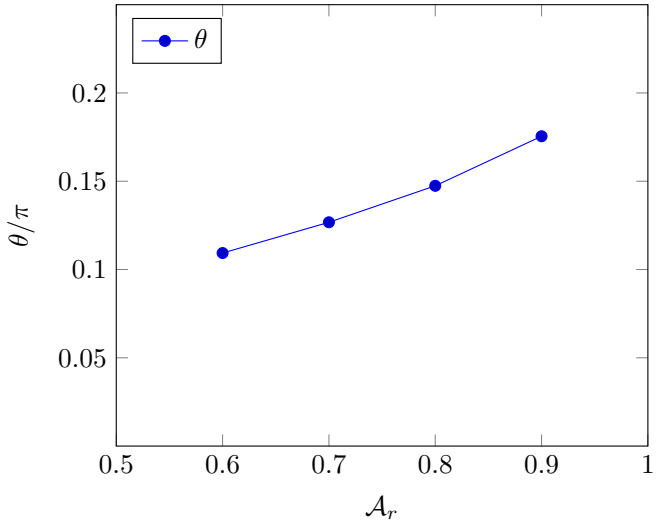

FIG. 1. (Color online) A plot of θ/π against $\mathcal{A}_r$ for $L = 20$, $W = 5$, $\Lambda = 1$, $\alpha^* = 0.01$, $\mathrm{Re} = 10^{-3}$; compare with Ref. [32, Fig. 1].

with the help of parametric meshes Γ^h, which are updated by the fluid velocity. Since the membrane surface is locally incompressible, it turns out that the surface mesh has good mesh properties during the evolution. This is in contrast to other fluid problems with interfaces in which the mesh often deteriorates during the evolution when updated with the fluid velocity; see, e.g., Ref. [55].

The nondimensionalized elastic forcing by the membrane curvature energy, $\vec{f}_\Gamma^*$ in Eq. (7), is discretized with the help of a weak formulation by Dziuk [18], which is generalized by Barrett *et al.* [46] to take spontaneous curvature and area difference elasticity effects into account. A main ingredient of the numerical approach is the fact that one can use a weak formulation of Eq. (5) that can be discretized in a stable way. In fact, defining $A^* = \beta^*[M(\Gamma) - M_0^*]$ and $\vec{y} = \vec{x} + (A^* - \overline{x}^*)\,\vec{\nu}$ the following identity, which has to hold for all $\vec{\chi}$ on Γ,

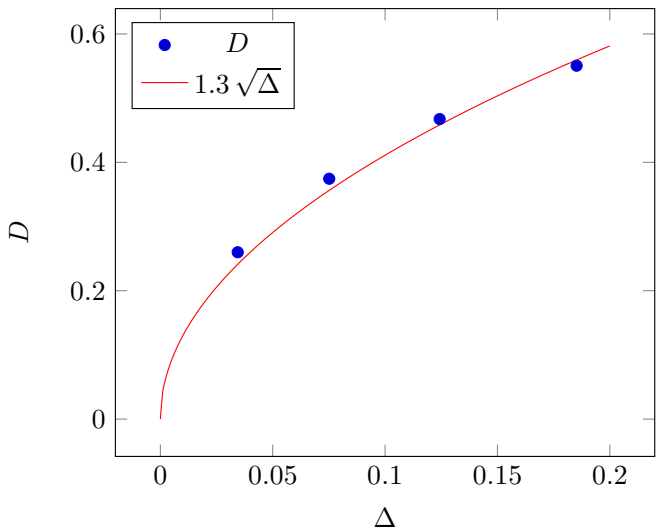

FIG. 2. (Color online) A plot of D against Δ for $L = 20$, $W = 5$, $\Lambda = 1$, $\alpha^* = 0.01$, $\mathrm{Re} = 10^{-3}$; compare with Ref. [32, Fig. 2].

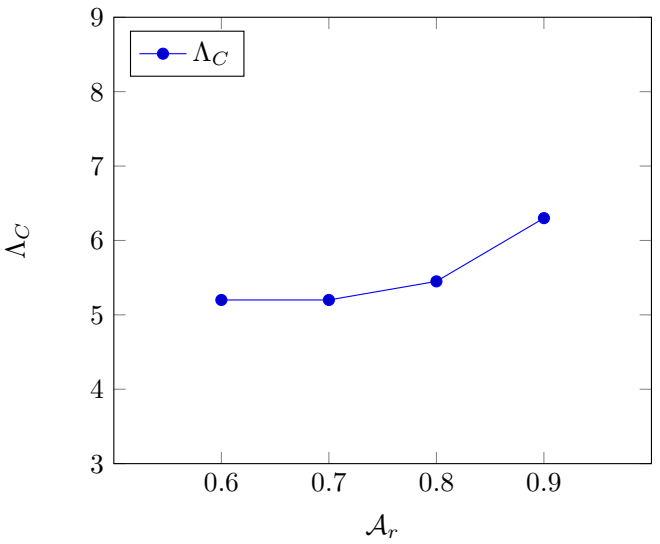

FIG. 3. (Color online) A plot of Λ_C against $\mathcal{A}_r$ for $L = 20$, $W = 5$, $\alpha^* = 0.01$, $\mathrm{Re} = 10^{-3}$; compare with Ref. [32, Fig. 3].

characterizes $\vec{f}_\Gamma^*$:

$$\begin{aligned}\langle \vec{f}_\Gamma^*, \vec{\chi}\rangle = {} & \langle \vec{\nabla}_s\, \vec{y}, \vec{\nabla}_s\, \vec{\chi}\rangle + \langle \vec{\nabla}_s \cdot \vec{y}, \vec{\nabla}_s \cdot \vec{\chi}\rangle \\ & - 2\langle (\vec{\nabla}_s\, \vec{y})^T, \underline{\underline{D}}_s(\vec{\chi})\,(\vec{\nabla}_s\, \mathrm{id})^T\rangle + (A^* - \overline{x}^*)\langle \vec{x}, [\vec{\nabla}_s\, \vec{\chi}]^T\, \vec{\nu}\rangle \\ & - \tfrac{1}{2}\langle [|\vec{x} - \overline{x}^*\, \vec{\nu}|^2 - 2\,(\vec{y} \cdot \vec{x})]\, \vec{\nabla}_s\, \mathrm{id}, \vec{\nabla}_s\, \vec{\chi}\rangle \\ & - A^* \langle (\vec{x} \cdot \vec{\nu})\, \vec{\nabla}_s\, \mathrm{id}, \vec{\nabla}_s\, \vec{\chi}\rangle.\end{aligned}$$

Here $\langle \cdot, \cdot \rangle$ is the L^2-inner product on Γ, and $\vec{\nabla}_s\, \vec{y} = (\partial_{s_j}\, y_i)_{i,j=1}^3$ with $(\partial_{s_1}, \partial_{s_2}, \partial_{s_3})^T = \vec{\nabla}_s$. Roughly speaking, the above identity shows that $\vec{f}_\Gamma^*$ has a divergence structure. We remark here that

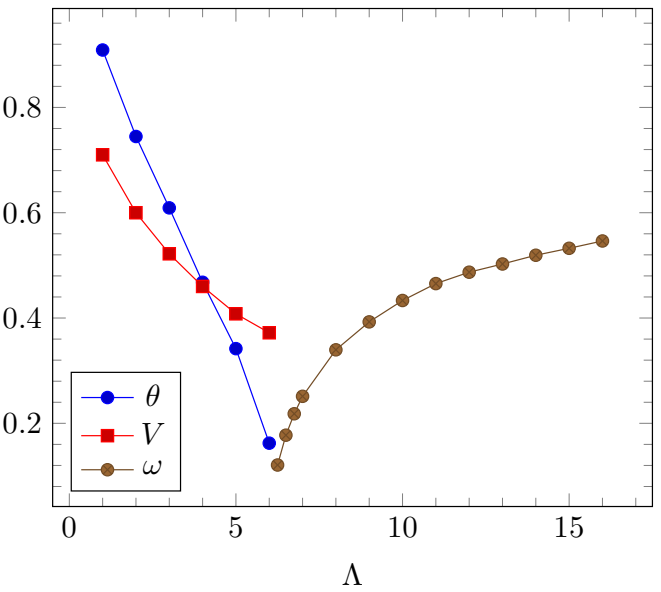

FIG. 4. (Color online) A plot of $\theta/\frac{\pi}{6}$, $V/\frac{1}{2}$, and $\omega/\frac{1}{2\pi}$ against Λ for $\mathcal{A}_r = 0.8$, $L = 11.55$, $W = 3.85$, $\alpha^* = 2$; compare with Ref. [67, Fig. 1].

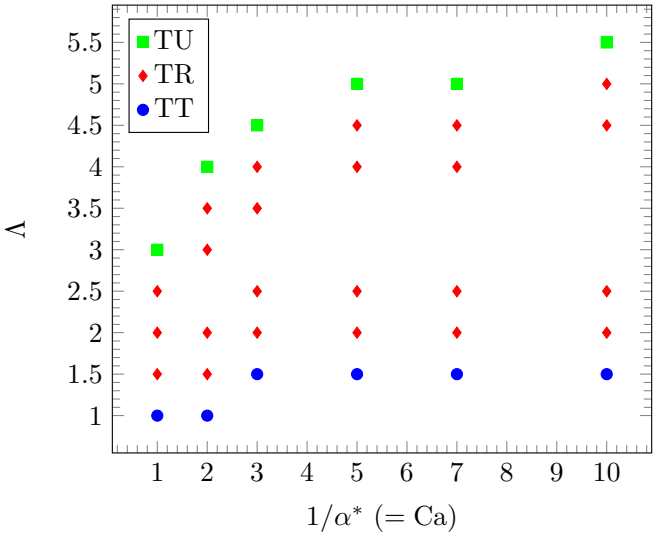

FIG. 5. (Color online) Analogue of the phase diagram from Ref. [54, Fig. 8] for the domain $\overline{\Omega} = [-3,3]^3$, starting with a prolate shape with $\mathcal{V}_r = 0.8$ and the longest axis in the x_3 direction.

similar divergence structures have been derived with the help of Noether's theorem; see Refs. [56,57].

The numerical method of Barrett *et al.* [46] has the feature that a semidiscrete, i.e., continuous in time and discrete in space, version of the method obeys a discrete analog of the energy inequality Eq. (3). In addition, this semidiscrete version has the property that the volume enclosed by the vesicle and the membrane's surface area are conserved exactly. After discretization in time these properties are approximately fulfilled to a high accuracy, see Sec. IV. The fully discrete system is linear and fully coupled in the unknowns. The overall system is reduced by a Schur complement approach to obtain a reduced system in just velocity and pressure unknowns. For this resulting linear system, well-known solution techniques for finite-element discretizations for the standard Navier-Stokes equations can be used; see Barrett *et al.* [58].

IV. NUMERICAL COMPUTATIONS

In shearing experiments the inclination angle of the vesicle in the shear-flow direction is often of interest. Here we will always consider shear flow in the x_1 direction with x_3 being the flow gradient direction. Precisely, if $\overline{\Omega} = [-L,L]^2 \times [-W,W]$, then we prescribe the inhomogeneous Dirichlet boundary condition $\vec{g}(\vec{x}) = (x_3,0,0)^T$ on the top and bottom boundaries $\partial_1\Omega = [-L,L]^2 \times \{\pm W\}$. Assuming the vesicle's center of mass is at the origin, then $\underline{\underline{M}} = \int_{\Omega_{-(t)}} |\vec{x}|^2 \underline{\underline{Id}} - \vec{x} \otimes \vec{x}\, dx$ denotes the vesicle's moment of inertia tensor. Let $\vec{p}$, with $|\vec{p}| = 1$ and $p_1 \geqslant 0$, be the eigenvector corresponding to the smallest eigenvalue of $\underline{\underline{M}}$. Then the vesicle's inclination angle is defined by $\theta = \arg(\overline{p_1} + \mathrm{i}\, p_3) \in (-\pi/2,\pi/2]$, where $\arg : \mathbb{C} \to (-\pi,\pi]$. For later use we also note that the deformation parameter D is defined by $(b-c)/(b+c)$, where b,c are the major and minor semiaxes of an ellipsoid with the same moment of inertia tensor; see, e.g., Ref. [59]. Hence, in 2D, $D = (\lambda_{\max}^{\frac{1}{2}} - \lambda_{\min}^{\frac{1}{2}})/(\lambda_{\max}^{\frac{1}{2}} + \lambda_{\min}^{\frac{1}{2}})$, where $\lambda_{\max}$ and $\lambda_{\min}$ are the two eigenvalues of $\underline{\underline{M}}$.

The inclination angle θ is important for the classification of different types of dynamics in the shear-flow experiments that we will present. The classical deformation dynamics for vesicles are the tank-treading (TT) and the tumbling (TU) motions. In the tank-treading motion the vesicle adopts a constant inclination angle in the flow, while the surface fluid rotates on the membrane surface. This motion is observed for small viscosity contrasts between the inner and the outer fluid and, as we will see later, at low surface membrane viscosity. At large viscosity contrasts or large membrane viscosity the tumbling motion occurs. In the tumbling regime the membrane rotates as a whole, and the inclination angle oscillates in the whole interval $(-\pi/2,\pi/2]$. In the past ten years a new dynamic regime for vesicles in shear flow has been identified. In this regime the inclination angle is neither constant nor does it oscillate in the whole interval $(-\pi/2,\pi/2]$. The dynamics are characterized by periodic oscillations of the inclination angle θ such that $\theta \in [-\theta_0,\theta_0]$ for a θ_0 in the open interval $(0,\pi/2)$. This regime was first predicted theoretically by Ref. [60] and subsequently observed experimentally in Ref. [61]. Later

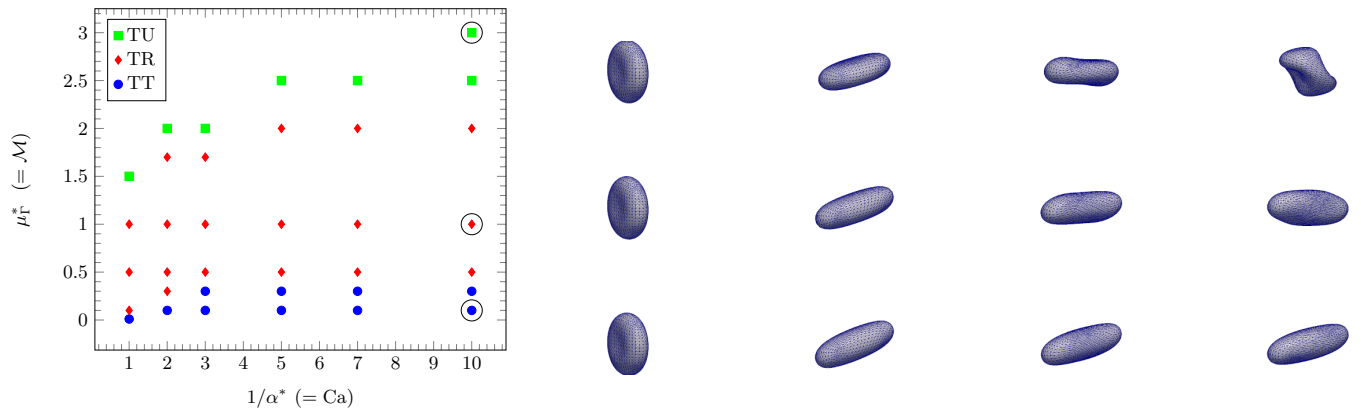

FIG. 6. (Color online) Phase diagram for $\Lambda = 1$ for the domain $\overline{\Omega} = [-3,3]^3$, starting with a biconcave shape with $\mathcal{V}_r = 0.8$ and the shortest axis in the x_1 direction. The three big circles in the phase diagram in (a) correspond to the simulations in (b), where from top to bottom we show the evolutions for $\mu_\Gamma^* = 3, 1, 0.1$ for $1/\alpha^* = 10$ at times $t = 0, 3, 6, 9$ (from left to right).

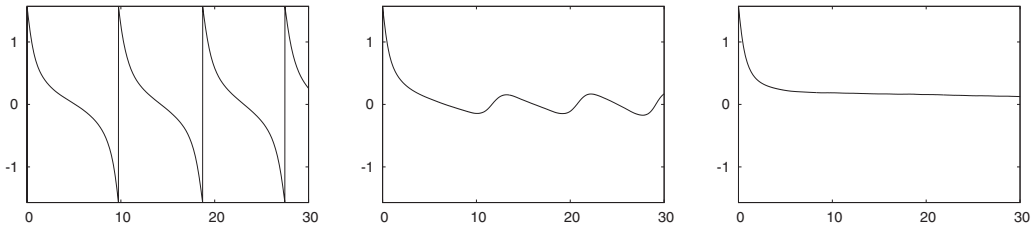

FIG. 7. The inclination angle θ, in radiant, plotted against time for the computations in Fig. 6. They correspond to the motions TU for $\mu_\Gamma^* = 3$ (a), TR for $\mu_\Gamma^* = 1$ (b), and TT for $\mu_\Gamma^* = 0.1$ (c), respectively.

this regime has been studied by different groups; see, e.g., Refs. [53,54,62–66] for more details. In Ref. [60] this motion was called vacillating-breathing, and later the same motion was also called trembling, transition mode, or swinging. Following Ref. [64] we will refer to this new regime as the transition (TR) mode.

In our numerical simulations we will only consider the scaling Eq. (7). For all the presented simulations we will state the reduced volume as a characteristic invariant. It is defined as $\mathcal{V}_r = 6\pi^{\frac{1}{2}}\mathcal{V}(0)/\mathcal{A}^{\frac{3}{2}}(0)$; see, e.g., Ref. [15]. Here $\mathcal{V}(t)$ and $\mathcal{A}(t)$ denote the volume of the discrete inner phase and the discrete surface area, respectively, at time t. Moreover, if nothing else is specified, then our numerical simulations are for no-slip boundary conditions; i.e., $\partial_1\Omega = \partial\Omega$ and $\vec{g} = \vec{0}$. In all our experiments it holds that $\overline{\varkappa}^*\,\beta^* = 0$, and we will only report the values of $\overline{\varkappa}^*$ and β^* for simulations where they are nonzero. Here we recall, as stated in the Introduction, that the energy

$$E^*(\Gamma) = \frac{1}{2}\int_\Gamma (\varkappa - \overline{\varkappa}^*)^2\, ds + \frac{\beta^*}{2}\,(M(\Gamma) - M_0^*)^2 \qquad (9)$$

for $\overline{\varkappa}^*\,\beta^* \neq 0$ is equivalent to Eq. (9) with $\overline{\varkappa}^* = 0$, the same value of $\beta^* > 0$, and a modified value of M_0^*. Finally, we stress that our sign convention for curvature is such that spheres have negative mean curvature.

A. 2D validation

In order to validate our numerical method, we reproduce some numerical results from Refs. [32,67], where we always consider a domain $\overline{\Omega} = [-L,L]\times[-W,W]$. As these works consider Navier-Stokes flow in the bulk, we consider Eq. (4) with $\mathrm{Re} = 10^{-3}$, $\mathrm{Re}_\Gamma = 0$, $\mu_\Gamma^* = \overline{\varkappa}^* = \beta^* = 0$, and vary Λ. For the comparison with Figs. 1–3 in Ref. [32] we also set $\alpha^* = 10^{-2}$. Moreover, we consider vesicles with reduced areas $\mathcal{A}_r = \frac{4\pi\mathcal{A}(0)}{P^2(0)} \in \{0.6,0.7,0.8,0.9\}$, and with $a = \frac{P(0)}{2\pi} = 1$, so

FIG. 8. (Color online) The vesicles for $\overline{\varkappa}^* = -5$ (a) and $\overline{\varkappa}^* = 5$ (b) at time $t = 0$.

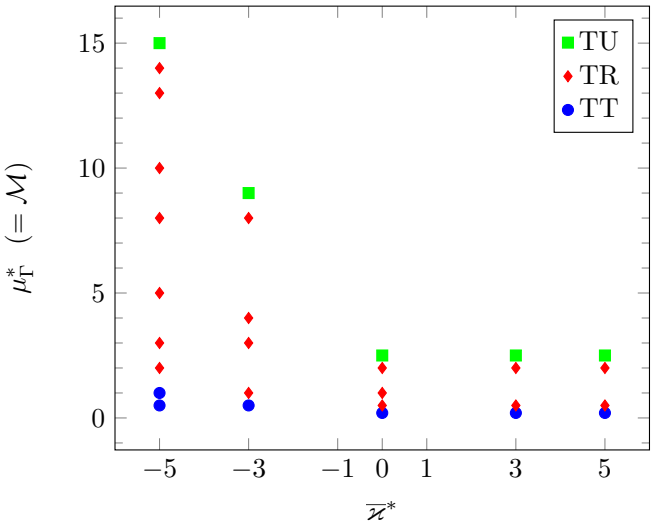

FIG. 9. (Color online) Phase diagram for $\mathrm{Ca} = 1/\alpha^* = 10$ for the domain $\overline{\Omega} = [-3,3]^3$, starting with biconcave shapes with $\mathcal{V}_r = 0.8$ and the shortest axis in the x_1 direction.

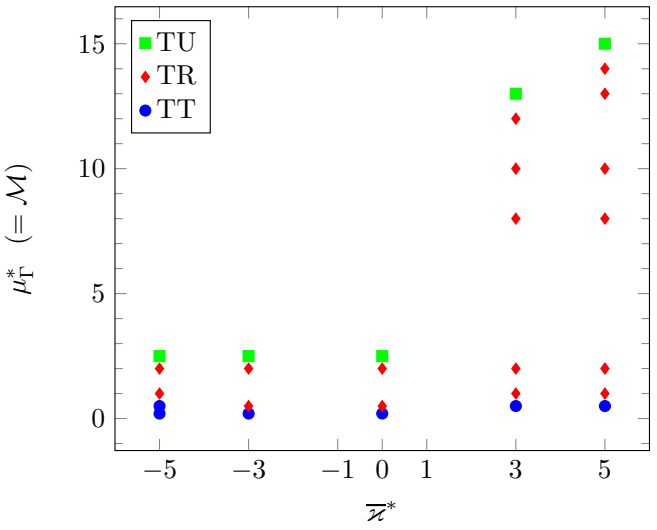

FIG. 10. (Color online) Phase diagram for $\mathrm{Ca} = 1/\alpha^* = 10$ for the domain $\overline{\Omega} = [-3,3]^3$, starting with biconcave shapes with $\mathcal{V}_r = 0.8$ and the shortest axis in the x_2 direction.

TABLE I. Some inclination angles θ for the TT motions in Fig. 9.

μ_Γ^*	$\overline{\varkappa}^* = -5$	$\overline{\varkappa}^* = 0$	$\overline{\varkappa}^* = 5$
0.05	0.179	0.178	0.194
0.1	0.169	0.158	0.179
0.2	0.161	0.116	0.138

TABLE II. Some inclination angles θ for the TT motions in Fig. 10.

μ_Γ^*	$\overline{\varkappa}^* = -5$	$\overline{\varkappa}^* = 0$	$\overline{\varkappa}^* = 5$
0.05	0.180	0.156	0.162
0.1	0.160	0.132	0.156
0.2	0.118	0.084	0.143

that perimeter and area are given by $P(0) = 2\pi$ and $\mathcal{A}(0) = \mathcal{A}_r\,\pi$, respectively. At first, for $\Lambda = 1$, we try to re-create

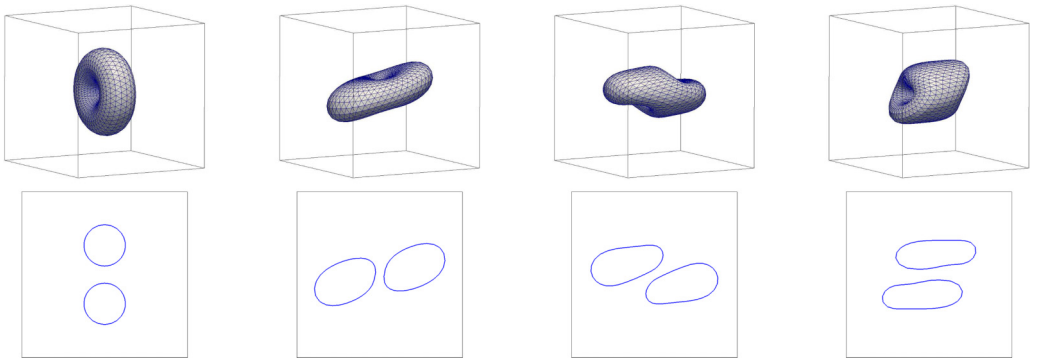

FIG. 11. (Color online) Shear flow for a torus with $\Lambda = \mu_\Gamma^* = 1$. The plots show the interface Γ^h within $\overline{\Omega}$, as well as cuts through the x_1-x_3 plane, at times $t = 0$, 2.5, 5, 7.5 (from left to right). The interface at $t = 10$ is very close to the plot at $t = 2.5$.

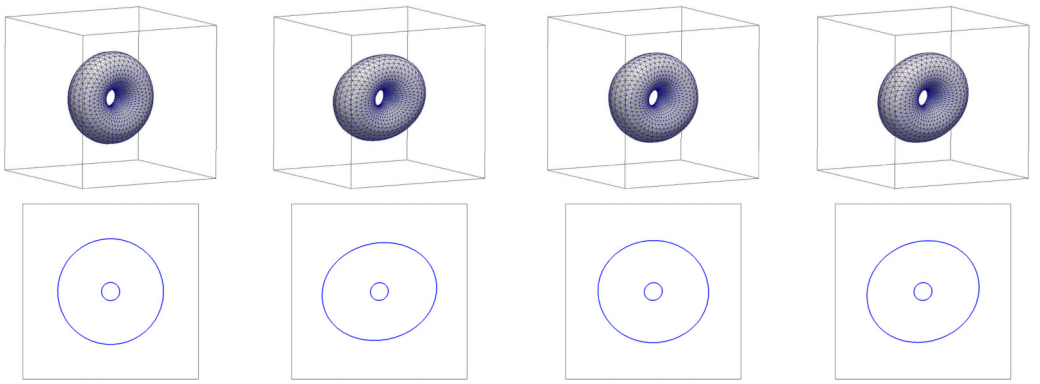

FIG. 12. (Color online) Shear flow for a torus with $\Lambda = 1$, $\mu_\Gamma^* = 10$. The plots show the interface Γ^h within $\overline{\Omega}$, as well as cuts through the x_1-x_3 plane, at times $t = 0$, 2.5, 5, 7.5 (from left to right).

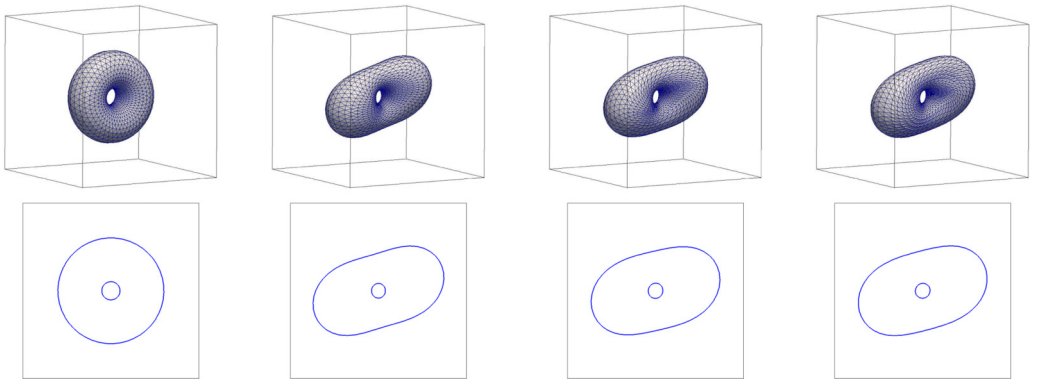

FIG. 13. (Color online) Shear flow for a torus with $\Lambda = 1$, $\mu_\Gamma^* = 0$. The plots show the interface Γ^h within $\overline{\Omega}$, as well as cuts through the x_1-x_3 plane, at times $t = 0$, 2.5, 5, 7.5 (from left to right).

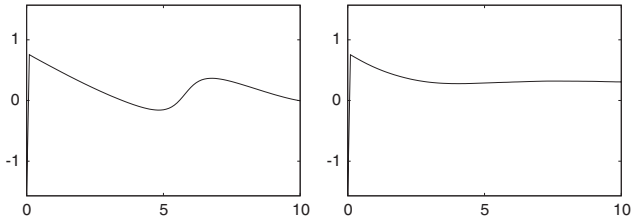

FIG. 14. The inclination angle θ, in radiant, plotted against time for the simulations in Figs. 12(a) and 13(b).

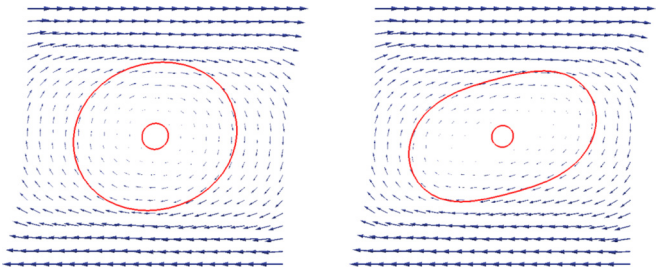

FIG. 15. (Color online) The flow at time $t = 7.5$ in the x_1-x_3 plane for the simulations in Figs. 12 and 13.

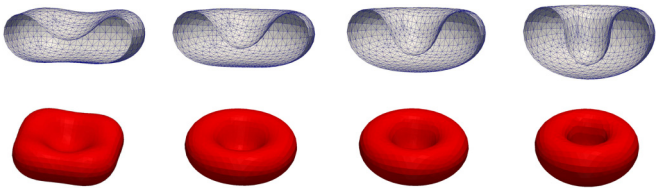

FIG. 16. (Color online) Flow for a cup-like stomatocyte shape with $\mathcal{V}_r = 0.65$ for $M_0^* = -48.24$ and $\beta^* = 0.053$. The plots show the interface Γ^h at times $t = 0$, 5, 10, 20 (from left to right), with the top row visualizing the triangulations by showing half the vesicle.

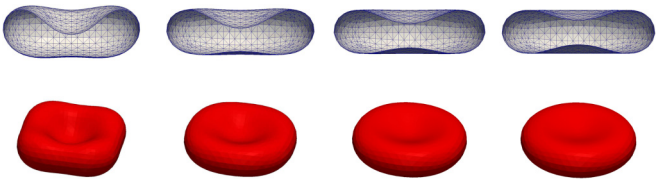

FIG. 17. (Color online) Same as Fig. 16 with $\beta^* = 0$.

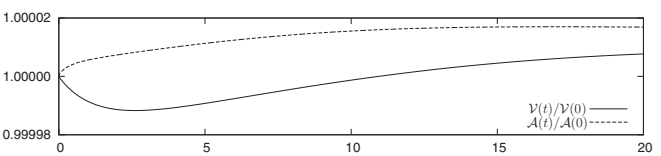

FIG. 18. The evolutions of the relative discrete volume $\mathcal{V}(t)/\mathcal{V}(0)$, and the relative discrete surface area $\mathcal{A}(t)/\mathcal{A}(0)$ over time.

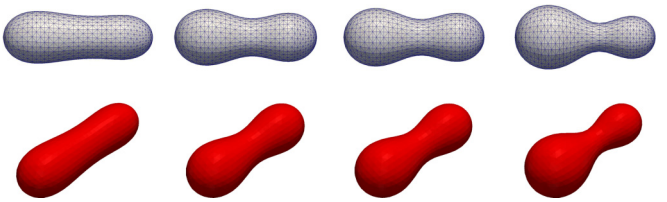

FIG. 19. (Color online) Flow for a varying-diameter cigar-like shape with $\mathcal{V}_r = 0.75$ for $M_0^* = -33.5$ and $\beta^* = 0.46$. The plots show the interface Γ^h at times $t = 0$, 1, 10, 50 (from left to right), with the top row visualizing the triangulations.

Ref. [32, Fig. 1]. To this end, we set $L = 20$ and $W = 5$, and use stress-free boundary conditions left and right, rather than periodic boundary conditions in the x_1 direction on the square domain $[-5,5]^2$ as used in Ref. [32]. We obtain the results in Fig. 1, where we plot θ/π against $\mathcal{A}_r$, which show a good agreement with Ref. [32, Fig. 1]. Similarly, in trying to re-create Ref. [32, Fig. 2] we also compute the deformation parameter D, and plot D against the excess length parameter $\Delta = 2\,(1 - \mathcal{A}_r^{\frac{1}{2}})/(\pi\,\mathcal{A}_r^{\frac{1}{2}})$. We obtain the results in Fig. 2, which show good agreement with Ref. [32, Fig. 2]. In Fig. 3 we plot the critical viscosity ratio Λ_C for the TT to TU transition against the reduced area $\mathcal{A}_r$. It should be noted that our numerical method produces larger values of Λ_C than reported in Ref. [32, Fig. 3].

Moreover, in trying to re-create Ref. [67, Fig. 1], we also ran with $\mathrm{Re} = 0.05$, $L = 11.55$, and $W = 3.85$, so that the restriction parameter χ as defined in Ref. [67] is $\chi = 0.26$. However, we note that periodic boundary conditions in the x_1 direction are used in Ref. [67], with the length L of the domain not clearly stated. We obtain the results in Fig. 4, where apart from θ, normalized by $\frac{\pi}{6}$, we also show the membrane tank-treading velocity $V = \frac{1}{P(0)} \int_\Gamma |\vec{u}|\, ds$, normalized by $\frac{1}{2}$, and the tumbling frequency ω, normalized by $\frac{1}{2\pi}$ (note that the frequency in Ref. [67, Fig. 1] is said to be normalized by $\frac{1}{4\pi}$). It should be noted that qualitatively our results agree well with Ref. [67, Fig. 1], but our numerical method produces a smaller value of Λ_C than reported in Ref. [67, Fig. 1].

Overall we are satisfied that our numerical method performs well. The observed differences with existing results in the literature can be explained by differences in the length of the domain, different boundary conditions, and different numerical methods used.

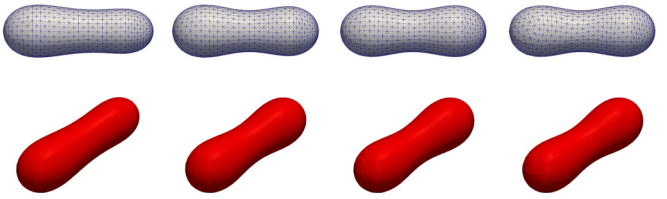

FIG. 20. (Color online) Same as Fig. 19 with $\beta^* = 0$.

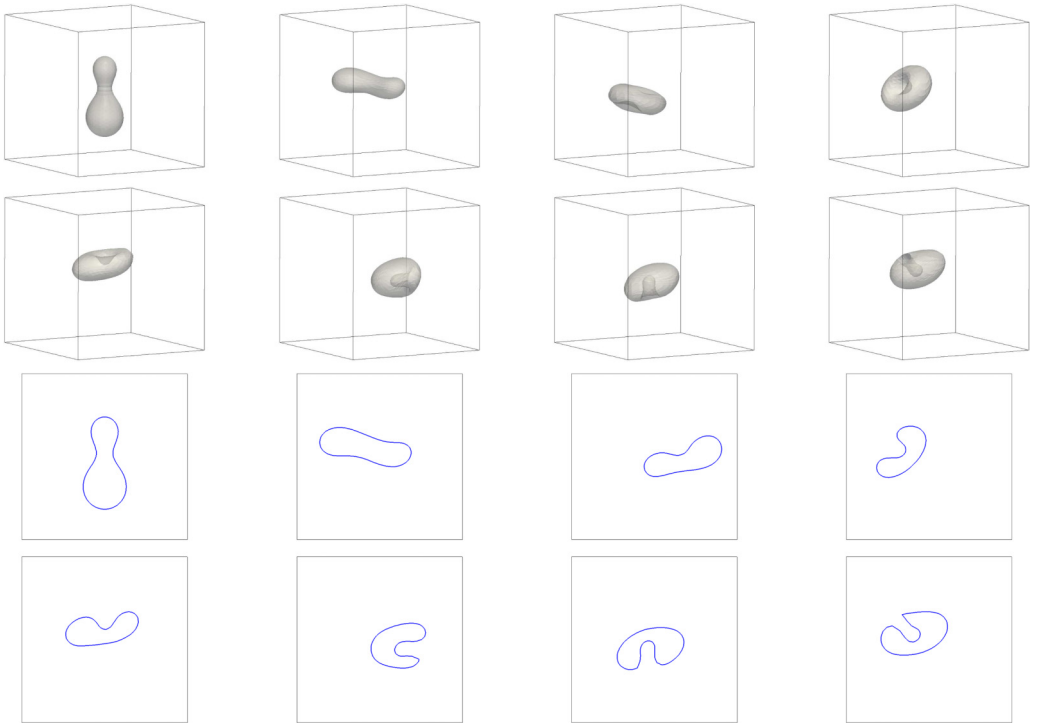

FIG. 21. (Color online) Shear flow for a budding shape with $\Lambda = \mu_\Gamma^* = 1$. Here $\beta^* = 0.1$ and $M_0^* = -33.5$. The first two rows show the interface Γ^h within $\overline{\Omega}$ at times $t = 0,\ 5,\ 15,\ 17.5$ (first row, from left to right) and $t = 20,\ 25,\ 27.5,\ 32.5$ (second row, from left to right). Similarly, the last two rows show cuts of Γ^h through the x_1-x_3 plane at the same times.

B. 3D validation

For a similar validation in 3D we compare our method to some numerical results from Ref. [54], where Stokes flow in an infinite domain is considered. In order to reproduce the phase diagram in Ref. [54, Fig. 8], which also contains numerical results from Ref. [66], we let $\overline{\Omega} = [-3,3]^3$ and choose the initial shape of the interface to be a prolate vesicle with a reduced volume of $\mathcal{V}_r = 0.8$ and a surface area of $\mathcal{A}(0) = 4\pi$, so that $S = 1$. The results from our algorithm are shown in Fig. 5. Due to finite-size effects, and the different boundary conditions, we observe different critical values for the phase transitions compared to Ref. [54, Fig. 8]. However, qualitatively our numerical method produces similar results.

C. Effect of surface viscosity

We consider the effect that surface viscosity has on the TT to TU transition. To this end, we let $\overline{\Omega} = [-3,3]^3$, and choose as initial shape of the vesicle a biconcave shape with reduced volume $\mathcal{V}_r = 0.8$ and $\mathcal{A}(0) = 4\pi$, so that $S = 1$. We let $\Lambda = 1$. In Fig. 6 we present a phase diagram with the axes labeled in terms of the nondimensional values $\mathrm{Ca} = \frac{1}{\alpha^*}$ and $\mathcal{M} = \mu_\Gamma^*$; recall Eq. (8) for $S = 1$. The evolutions for $\alpha^* = 0.1$, and either $\mu_\Gamma^* = 3$, $\mu_\Gamma^* = 1$, or $\mu_\Gamma^* = 0.1$, are visualized in Fig. 6, where we observe the motions TU, TR, and TT, respectively. We stress that the tumbling occurs for a viscosity contrast of $\Lambda = 1$, and so is only due to the chosen high surface viscosity μ_Γ^*. The fact that vesicles undergo a transition from steady tank-treading to unsteady tumbling motion has been observed earlier by Ref. [68], where, however, the authors used a particle-based mesoscopic model to analyze the fluid vesicle dynamics. A plot of the inclination angle θ for the simulations in Fig. 6 can be seen in Fig. 7.

D. Effect of spontaneous curvature

Here the initial shapes of the vesicles, for a reduced volume of $\mathcal{V}_r = 0.8$ and surface area $\mathcal{A}(0) = 4\pi$, so that $S = 1$, were chosen to be numerical approximations of local minimizers for the curvature energy $\int_\Gamma (\varkappa - \overline{\varkappa}^*)^2\, ds$. These discrete local minimizers were obtained with the help of the gradient flow scheme from Ref. [19], and for the choices $\overline{\varkappa}^* = \pm 5$ they are displayed in Fig. 8. For $\mathrm{Ca} = 1/\alpha^* = 10$ we show a phase diagram of $\mathcal{M} = \mu_\Gamma^*$ versus $\overline{\varkappa}^*$ in Fig. 9, where the initial vesicles are aligned such that their shortest axis is in the x_1 direction. Similarly, in Fig. 10 we show a phase diagram of $\mathcal{M} = \mu_\Gamma^*$ versus $\overline{\varkappa}^*$ when the initial vesicles are aligned such that their shortest axis is in the x_2 direction. The results in Figs. 9 and 10 indicate that the values of the surface viscosity, at which the transitions between TT, TR, and TU take place, strongly depend on the spontaneous curvature as well as on the orientation of the initial vesicle. As in Ref. [68], where the case $\overline{\varkappa}^* = 0$ was studied, we also observe that the inclination angle in the tank-treading motion decreases as μ_Γ^* increases; see Tables I and II.

E. Shearing for a torus

Here we use as the initial shape a Clifford torus, which is aligned with the x_2-x_3 plane, with reduced volume $\mathcal{V}_r = 0.71$

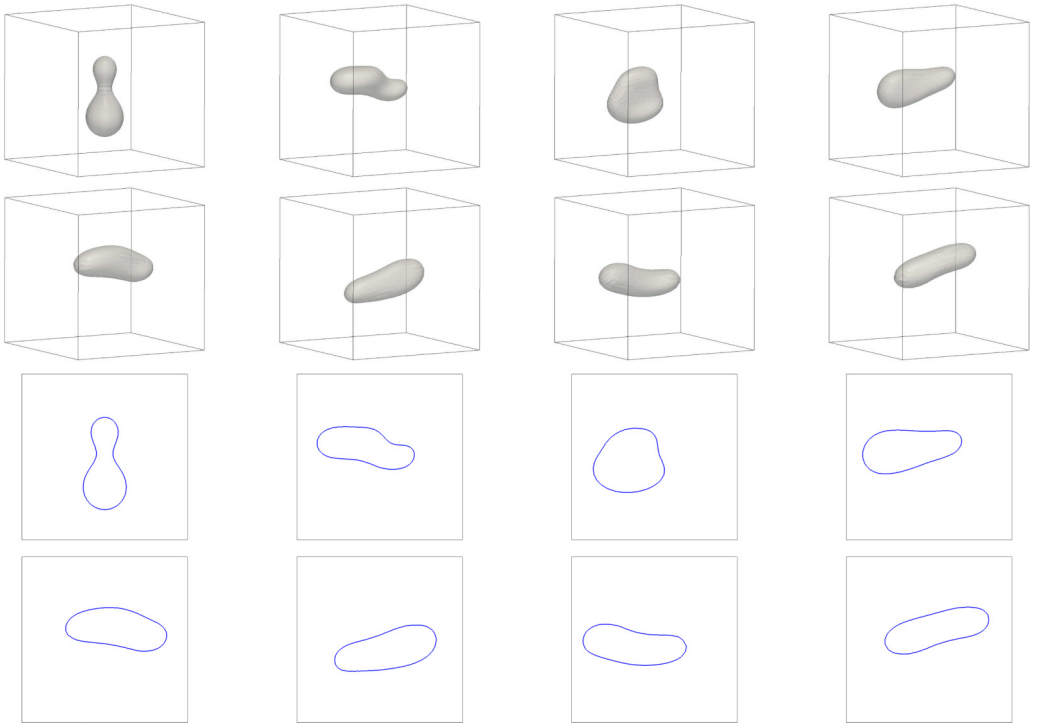

FIG. 22. (Color online) Same as Fig. 21 but with $\beta^* = 0$.

and $\mathcal{A}(0) = 13.88$, so that $S = 1.05$. We let $\Lambda = \mu_\Gamma^* = 1$, $\alpha^* = 0.05$ and use the domain $\overline{\Omega} = [-2,2]^3$; see Fig. 11, where the torus appears to tumble while undergoing strong deformations.

Repeating the experiment for an initial torus aligned with the shear flow direction, and setting $\alpha^* = 1$ and $\mu_\Gamma^* = 10$, leads to the results shown in Fig. 12. This shows a TR motion. Setting $\mu_\Gamma^* = 0$, on the other hand, leads to TT, as shown in Fig. 13. A plot of the inclination angle θ for the simulations in Figs. 12 and 13 can be seen in Fig. 14, while we visualize the flow in the x_1-x_3 plane in Fig. 15.

F. Effect of area difference elasticity

We consider $\overline{\Omega} = [-4,4]^3$ and set $\Lambda = \mu_\Gamma^* = \alpha^* = 1$. The parameters for $\vec{f}_\Gamma^*$ are $\beta^* = 0.053$ and $M_0^* = -48.24$. For the vesicle we use a cup-like stomatocyte initial shape with $\mathcal{V}_r = 0.65$ and $\mathcal{A}(0) = 82.31$, so that $S = 2.56$. See Fig. 16 for a numerical simulation. As a comparison, we show the same simulation with $\beta^* = 0$ in Fig. 17.

In Fig. 18 we show the evolutions of the discrete volume of the inner phase and the discrete surface area over time. Clearly these two quantities are preserved almost exactly for our numerical scheme in this simulation. In fact, a semidiscrete variant of our scheme conserves these two quantities exactly, and so in practice the fully discrete algorithm will preserve them well for sufficiently small time-step sizes.

In our next simulation, we let $\overline{\Omega} = [-2.5,2.5]^3$ and set $\Lambda = \alpha^* = 1$, as well as $\beta^* = 0.46$ and $M_0^* = -33.5$. As initial vesicle we take a varying-diameter cigar-like shape that has $\mathcal{V}_r = 0.75$ and $\mathcal{A}(0) = 9.65$, so that $S = 0.88$. A simulation can be seen in Fig. 19. As a comparison, we show the simulation with $\beta^* = 0$ in Fig. 20. Similarly to previous studies, where an energy involving area difference elasticity

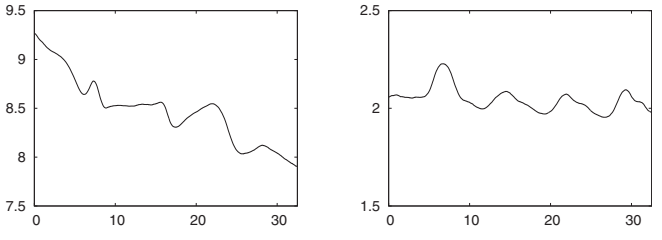

(a) (b)

FIG. 23. The bending energy $\alpha^* E^*(\Gamma^h)$ plotted against time for the computations in Figs. 21(a) and 22(b).

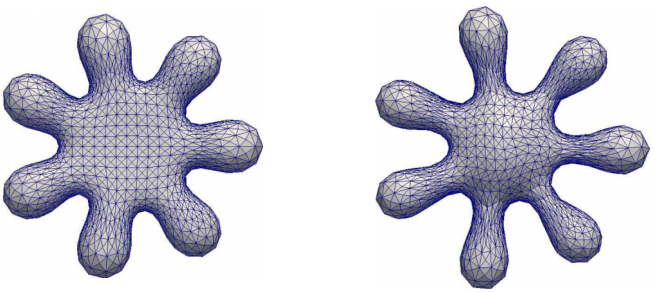

(a) (b)

FIG. 24. (Color online) Flow for a seven-arm figure with $\mathcal{V}_r = 0.38$. Here $\beta^* = 0.05$ and $M_0^* = 180$. The triangulations Γ^h at times $t = 0$ (a) and 5 (b).

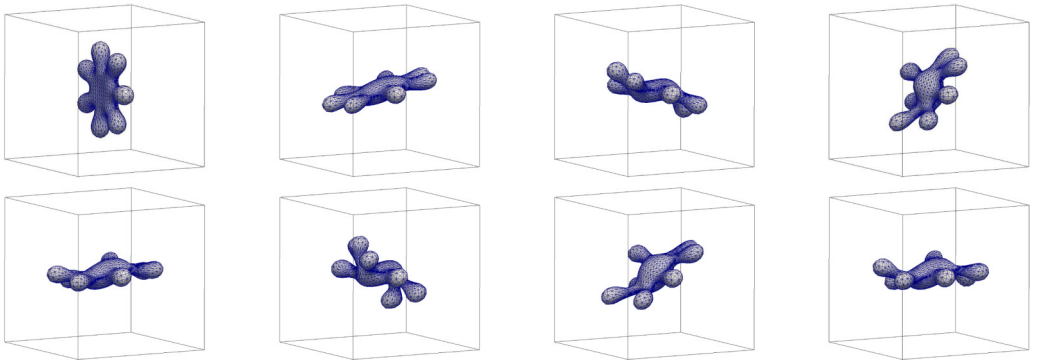

FIG. 25. (Color online) Shear flow for a budding shape with $\Lambda = \mu_\Gamma^* = 1$. Here $\beta^* = 0.05$ and $M_0^* = 180$. The plots show the interface Γ^h within $\overline{\Omega}$ at times $t = 0$, 2.5, 5, 7.5 (first row, from left to right) and $t = 10$, 12.5, 15, 17.5 (second row, from left to right).

terms was minimized, we also observe in our hydrodynamic model that less symmetric shapes occur when the ADE-energy contributions are taken into account.

G. Shearing for budded shape (two arms)

We start a scaled variant of the final shape from Fig. 19 in a shear flow experiment in $\overline{\Omega} = [-2,2]^3$. In particular, the initial shape is axisymmetric, with reduced volume $\mathcal{V}_r = 0.75$ and $\mathcal{A}(0) = 5.43$, so that $S = 0.66$. We set $\Lambda = \mu_\Gamma^* = 1, \alpha^* = 0.05$; see Fig. 21 for a run with $\beta^* = 0.1$ and $M_0^* = -33.5$. We observe that the shape of the vesicle changes drastically, with part of the surface growing inwards. This is similar to the shapes observed in Fig. 16, where the presence of a lower reduced volume led to cup-like stomatocyte shapes. We repeat the same experiment for $\beta^* = 0$ in Fig. 22. Now the budding shape loses its strong nonconvexity completely, as can be clearly seen in the plots of the two-dimensional cuts in Fig. 22. Plots of the bending energy $\alpha^* E^*(\Gamma^h)$ are shown in Fig. 23, where we recall that the energy inequality in Eq. (3) does not hold for the inhomogeneous boundary conditions employed in the present simulations.

H. Shearing for a seven-arm starfish

We consider simulations for a scaled version of the final shape from Barrett *et al.* [19, Fig. 23] with reduced volume $\mathcal{V}_r = 0.38$ and $\mathcal{A}(0) = 10.54$, so that $S = 0.92$, inside the domain $\overline{\Omega} = [-2,2]^3$. We set $\Lambda = \mu_\Gamma^* = \alpha^* = 1$. In order to maintain the seven-arm shape during the evolution we set $\beta^* = 0.05$ and $M_0^* = 180$. The first experiment is for no-slip boundary conditions on $\partial\Omega$ and shows that the seven arms grow slightly; see Fig. 24. If we use the shear flow boundary conditions, on the other hand, we observe the behavior in Fig. 25, where we have changed the value of α^* to 0.05. The vesicle can be seen tumbling, with a tumbling period of about 7, with the seven arms remaining intact throughout. Repeating the same experiment with $\beta^* = 0$ yields the simulation in Fig. 26. Not surprisingly, some of the arms of the vesicle are disappearing. We also tried to investigate whether the arms enhance or inhibit the tumbling behavior of the vesicle. To this end, we repeated the simulation in Fig. 25 for an ellipsoidal vesicle with the same reduced volume and surface area. This vesicle also exhibited TU with a tumbling period of about 7, so there was no significant change to the behavior in Fig. 25.

V. CONCLUSIONS

We have introduced a parametric finite-element method for the evolution of bilayer membranes by coupling a general curvature elasticity model for the membrane to (Navier-)Stokes systems in the two bulk phases and to a surface (Navier-)Stokes system. The model is based on work by Arroyo and DeSimone [43], which we generalized such that ADE effects are taken into account. Our main purpose was to study the influence of the area difference elasticity and of the spontaneous curvature on

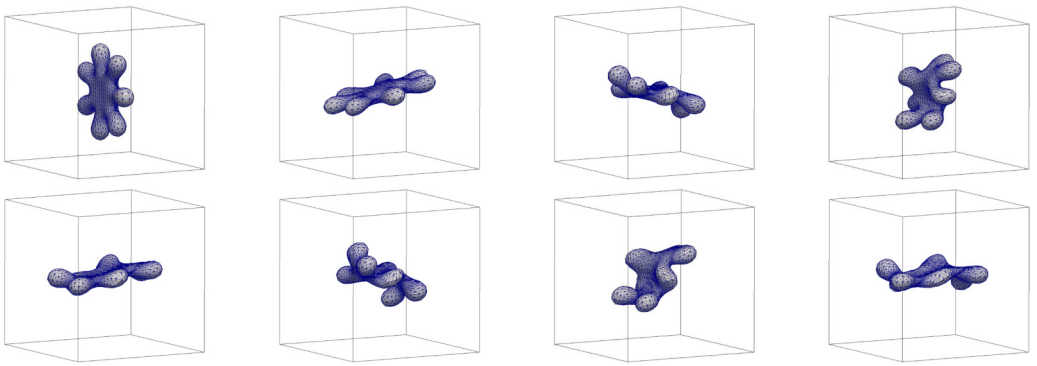

FIG. 26. (Color online) Same as Fig. 25 with $\beta^* = 0$.

the evolution of the membrane. In contrast to most other works, we discretized the full-bulk (Navier-)Stokes systems coupled to the surface (Navier-)Stokes system and coupled this to a bending energy involving ADE and spontaneous curvature.

The numerical simulations led to the following findings.

(1) The proposed numerical method conserves the volume enclosed by the membrane and the surface area of the membrane to a high precision.

(2) The transition from a tank-treading (TT) motion to a transition motion (TR) and to a tumbling (TU) motion depended strongly on the surface viscosity. We observed that the surface viscosity alone with no viscosity contrast between inner and outer fluid can lead to a transition from tank treading to a TR motion and to tumbling. Similar observations have been reported by Ref. [68] using a particle-based method.

(3) The surface viscosity at which a transition between the different motions TT, TR, and TU occur, strongly depends on the spontaneous curvature and on the initial alignment of the vesicle. In particular, we observed that for negative spontaneous curvature and an initial biconcave vesicle aligned such that the shortest axis is in the shear-flow direction all transitions occurred for larger values of the surface viscosity. For this alignment, and for positive spontaneous curvature, we observed that tumbling occurred already for much smaller values of the surface viscosity. The reverse was true for an alternative alignment. Here we recall that our sign convention for curvature means that spheres have negative mean curvature.

(4) In some cases, shear flow can lead to drastic shape changes, in particular for the ADE model. For example, we observed the transition of a budded pear-like shape to a cup-like stomatocyte shape in shear flow if an ADE model was used for the curvature elasticity.

(5) The ADE model can also lead to starfish-type shapes with several arms; see, e.g., Refs. [1,15]. In computations for a seven-arm starfish for a model involving an ADE-type energy, we observed that in shear flow the overall structure seems to be quite robust. In particular, the seven arms deformed but remained present even in a tumbling motion. However, arms tend to disappear if the area difference elasticity term is neglected.

Thus, we have shown that the proposed numerical method is a robust tool to simulate bilayer membranes for quite general models, which in particular take the full hydrodynamics and a curvature model involving area difference elasticity and spontaneous curvature into account.

ACKNOWLEDGMENTS

The authors gratefully acknowledge the support of the Deutsche Forschungsgemeinschaft via Grant No. SPP 1506, entitled "Transport processes at fluidic interfaces," and of the Regensburger Universitätsstiftung Hans Vielberth.

[1] U. Seifert, Adv. Phys. **46**, 13 (1997).
[2] T. Baumgart, S. T. Hess, and W. W. Webb, Nature **425**, 821 (2003).
[3] H. Noguchi and G. Gompper, Proc. Natl. Acad. Sci. USA **102**, 14159 (2005).
[4] J. L. McWhirter, H. Noguchi, and G. Gompper, Proc. Natl. Acad. Sci. USA **106**, 6039 (2009).
[5] P. Canham, J. Theor. Biol. **26**, 61 (1970).
[6] W. Helfrich, Z. Naturforsch. **28**, 693 (1973).
[7] S. Martens and H. T. McMahon, Nat. Rev. Mol. Cell. Biol. **9**, 543 (2008).
[8] M. M. Kamal, D. Mills, M. Grzybek, and J. Howard, Proc. Natl. Acad. Sci. USA **106**, 22245 (2009).
[9] S. Svetina, A. Ottova-Leitmannová, and R. Glaser, J. Theor. Biol. **94**, 13 (1982).
[10] S. Svetina and B. Zeks, Biomed. Biochim. Acta **42**, 86 (1983).
[11] S. Svetina and B. Žekš, Eur. Biophys. J. **17**, 101 (1989).
[12] L. Miao, U. Seifert, M. Wortis, and H.-G. Döbereiner, Phys. Rev. E **49**, 5389 (1994).
[13] P. Ziherl and S. Svetina, Europhys. Lett. **70**, 690 (2005).
[14] U. Seifert, K. Berndl, and R. Lipowsky, Phys. Rev. A **44**, 1182 (1991).
[15] W. Wintz, H.-G. Döbereiner, and U. Seifert, Europhys. Lett. **33**, 403 (1996).
[16] U. F. Mayer and G. Simonett, Interfaces Free Bound. **4**, 89 (2002).
[17] U. Clarenz, U. Diewald, G. Dziuk, M. Rumpf, and R. Rusu, Comput. Aided Geom. Design **21**, 427 (2004).
[18] G. Dziuk, Numer. Math. **111**, 55 (2008).
[19] J. W. Barrett, H. Garcke, and R. Nürnberg, SIAM J. Sci. Comput. **31**, 225 (2008).
[20] Q. Du, C. Liu, R. Ryham, and X. Wang, Nonlinearity **18**, 1249 (2005).
[21] M. Franken, M. Rumpf, and B. Wirth, Int. J. Numer. Anal. Model. **10**, 116 (2013).
[22] A. Bonito, R. H. Nochetto, and M. S. Pauletti, J. Comput. Phys. **229**, 3171 (2010).
[23] Q. Du, C. Liu, and X. Wang, J. Comput. Phys. **198**, 450 (2004).
[24] C. M. Elliott and B. Stinner, J. Comput. Phys. **229**, 6585 (2010).
[25] S. Bartels, G. Dolzmann, R. H. Nochetto, and A. Raisch, Interfaces Free Bound. **14**, 231 (2012).
[26] M. Mercker, A. Marciniak-Czochra, T. Richter, and D. Hartmann, SIAM J. Appl. Math. **73**, 1768 (2013).
[27] Q. Du, C. Liu, R. Ryham, and X. Wang, Phys. D **238**, 923 (2009).
[28] G. Boedec, M. Leonetti, and M. Jaeger, J. Comput. Phys. **230**, 1020 (2011).
[29] M. Rahimi and M. Arroyo, Phys. Rev. E **86**, 011932 (2012).
[30] D. S. Rodrigues, R. F. Ausas, F. Mut, and G. C. Buscaglia, J. Comput. Phys. **298**, 565 (2015).
[31] D. Salac and M. Miksis, J. Comput. Phys. **230**, 8192 (2011).
[32] D. Salac and M. J. Miksis, J. Fluid Mech. **711**, 122 (2012).
[33] A. Laadhari, P. Saramito, and C. Misbah, J. Comput. Phys. **263**, 328 (2014).
[34] V. Doyeux, Y. Guyot, V. Chabannes, C. Prud'homme, and M. Ismail, J. Comput. Appl. Math. **246**, 251 (2013).

[35] T. Biben, K. Kassner, and C. Misbah, Phys. Rev. E **72**, 041921 (2005).
[36] D. Jamet and C. Misbah, Phys. Rev. E **76**, 051907 (2007).
[37] S. Aland, S. Egerer, J. Lowengrub, and A. Voigt, J. Comput. Phys. **277**, 32 (2014).
[38] Y. Kim and M.-C. Lai, J. Comput. Phys. **229**, 4840 (2010).
[39] Y. Kim and M.-C. Lai, Phys. Rev. E **86**, 066321 (2012).
[40] W.-F. Hu, Y. Kim, and M.-C. Lai, J. Comput. Phys. **257**, 670 (2014).
[41] W. R. Dodson and P. Dimitrakopoulos, Phys. Rev. E **84**, 011913 (2011).
[42] A. Farutin, T. Biben, and C. Misbah, J. Comput. Phys. **275**, 539 (2014).
[43] M. Arroyo and A. DeSimone, Phys. Rev. E **79**, 031915 (2009).
[44] M. Arroyo, A. DeSimone, and L. Heltai, (2010), arXiv:1007.4934.
[45] J. W. Barrett, H. Garcke, and R. Nürnberg, "A stable numerical method for the dynamics of fluidic biomembranes" (2014), preprint No. 18/2014, University Regensburg, Germany.
[46] J. W. Barrett, H. Garcke, and R. Nürnberg, "Finite element approximation for the dynamics of asymmetric fluidic biomembranes" (2015), preprint No. 03/2015, University Regensburg, Germany.
[47] U. Seifert, L. Miao, H.-G. Döbereiner, and M. Wortis, in *The Structure and Conformation of Amphiphilic Membranes*, Springer Proceedings in Physics, Vol. 66, edited by R. Lipowsky, D. Richter, and K. Kremer (Springer-Verlag, Berlin, 1992), pp. 93–96.
[48] W. Wiese, W. Harbich, and W. Helfrich, J. Phys. Condens. Matter **4**, 1647 (1992).
[49] B. Bozic, S. Svetina, B. Zeks, and R. Waugh, Biophys. J. **61**, 963 (1992).
[50] L. E. Scriven, Chem. Eng. Sci. **12**, 98 (1960).
[51] T. J. Willmore, An. Şti. Univ. "Al. I. Cuza" Iaşi Secţ. I a Mat. (N. S.) B **11**, 493 (1965).
[52] M. Faivre, Drops, vesicles and red blood cells: Deformability and behavior under flow, Ph.D. thesis, Université Joseph Fourier, Grenoble, France, 2006.
[53] D. Abreu, M. Levant, V. Steinberg, and U. Seifert, Adv. Colloid Interface Sci. **208**, 129 (2014).
[54] A. P. Spann, H. Zhao, and E. S. G. Shaqfeh, Phys. Fluids **26**, 031902 (2014).
[55] E. Bänsch, Numer. Math. **88**, 203 (2001).
[56] R. Capovilla and J. Guven, J. Phys. Condens. Matter **16**, 2187 (2004).
[57] D. Lengeler (2015), arXiv.1506.08991.
[58] J. W. Barrett, H. Garcke, and R. Nürnberg, J. Sci. Comp. **63**, 78 (2015).
[59] S. Ramanujan and C. Pozrikidis, J. Fluid Mech. **361**, 117 (1998).
[60] C. Misbah, Phys. Rev. Lett. **96**, 028104 (2006).
[61] V. Kantsler and V. Steinberg, Phys. Rev. Lett. **96**, 036001 (2006).
[62] N. J. Zabusky, E. Segre, J. Deschamps, V. Kantsler, and V. Steinberg, Phys. Fluids **23**, 041905 (2011).
[63] H. Noguchi and G. Gompper, Phys. Rev. Lett. **98**, 128103 (2007).
[64] A. Yazdani and P. Bagchi, Phys. Rev. E **85**, 056308 (2012).
[65] A. Farutin and C. Misbah, Phys. Rev. Lett. **109**, 248106 (2012).
[66] T. Biben, A. Farutin, and C. Misbah, Phys. Rev. E **83**, 031921 (2011).
[67] B. Kaoui, T. Krüger, and J. Harting, Soft Matter **8**, 9246 (2012).
[68] H. Noguchi and G. Gompper, Phys. Rev. E **72**, 011901 (2005).